UC Berkeley
UC Berkeley Previously Published Works

Title
Directed Assembly of Nanoparticle Catalysts on Nanowire Photoelectrodes for Photoelectrochemical CO2 Reduction

Permalink
https://escholarship.org/uc/item/7c77t18n

Journal
Nano Letters, 16(9)

ISSN
1530-6984

Authors
Kong, Qiao
Kim, Dohyung
Liu, Chong
et al.

Publication Date
2016-09-14

DOI
10.1021/acs.nanolett.6b02321

Peer reviewed

Directed assembly of nanoparticle catalysts on

nanowire photoelectrodes for photoelectrochemical CO₂ reduction

Authors:

Qiao Kong[1, †], Dohyung Kim[2, †], Chong Liu[1,3], Yi Yu[1], Yude Su[1], Yifan Li[1], Peidong Yang[1,2,3,4*]

Affiliations:

[1] Department of Chemistry, University of California, Berkeley, CA 94720, USA

[2] Department of Materials Science and Engineering, University of California, Berkeley, CA 94720, USA

[3] Materials Sciences Division, Lawrence Berkeley National Laboratory, Berkeley, CA 94720, USA

[4] Kavli Energy Nanosciences Institute, Berkeley, CA 94720, USA

[†] These authors contributed equally to this work.

[*] To whom correspondence should be addressed. Email: p_yang@berkeley.edu

Reducing carbon dioxide with a multi-component artificial photosynthetic system, closely mimicking nature, represents a promising approach for energy storage[1-8]. Previous works have focused on exploiting light-harvesting semiconductor nanowires (NW) for photoelectrochemical water splitting[9-12]. With the newly developed CO_2 reduction nanoparticle (NP) catalysts[13-15], direct interfacing of these nanocatalysts with NW light absorbers for photoelectrochemical reduction of CO_2 becomes feasible. Here, we demonstrate a directed assembly of NP catalysts on vertical NW substrates for CO_2-to-CO conversion under illumination. Guided by the one-dimensional geometry, well-dispersed assembly of Au_3Cu NPs on the surface of Si NW arrays was achieved with facile coverage tunability. Such Au_3Cu NP decorated Si NW arrays can readily serve as effective CO_2 reduction photoelectrodes, exhibiting high CO_2-to-CO selectivity close to 80% at -0.20 V vs RHE with suppressed hydrogen evolution. A reduction of 120 mV overpotential compared to the planar counterpart was observed resulting from the optimized spatial arrangement of NP catalysts on the high surface area NW arrays. In addition, this system showed consistent photoelectrochemical CO_2 reduction capability up to 18hrs. This simple photoelectrode assembly process will lead to further progress in artificial photosynthesis, by allowing the combination of developments in each sub-field to create an efficient light-driven system generating carbon-based fuels.

2

Artificial photosynthesis is a promising energy storage method that converts solar energy to energy stored in chemical bonds[1,2]. As the name suggests, it mimics nature's energy cycle and shares some common features of complexity regarding the multiple processes involved. Photosynthesis, in general, consists of the light harvesting part, where the absorbed photons are converted to charge carriers, and the catalytic conversion part, where the charge carriers are subsequently used to drive targeted reactions. In order to assemble an efficient photosynthetic system, the utmost performance of the individual components is required as well as the optimized spatial arrangement between the components. Previous research has mainly focused on advancing solar water splitting reactions, in which efficient semiconductor light absorbers and hydrogen evolving catalysts have been combined[9,16-20]. Recently, a few studies have been reported for photoelectrochemical CO_2 reduction by integrating catalytic components using various methods including photoelectrodeposition, atomic layer deposition, etc[3,7,8,21,22]. With the latest advances in discovering efficient CO_2 reducing NP electrocatalysts that have the potential to be light-driven[13-15], it is necessary to develop an effective process for integrating these nanocatalysts with well-studied light absorbers.

Directed assembly of NP catalysts on NW light absorbers is demonstrated here to create an integrated photoelectrode for photoelectrochemical reduction of CO_2. TiO_2-protected n^+p-Si NW arrays were fabricated (Extended Data Figure 1), in parallel with a Au_3Cu NP catalyst (Extended Data Figure 2) featuring high turnover and mass activity for CO_2-to-CO conversion reported previously from our lab[14], as CO is one of the attractive targets in artificial photosynthesis[23]. Photoelectrochemical production of CO in aqueous environments is appealing as it enables generation of syngas using a renewable

3

energy source[24,25]. Syngas produced in this manner can serve as a basis for a variety of commodity chemicals converted at the downstream[26].

In a simple drop-casting process, the NW geometry allows the NP solutions to dry in a unidirectional manner with a receding meniscus along the wires, and as a result the NPs are being uniformly decorated onto the NW surface (Figure 1a, b). This feature is in stark contrast to what is typically observed on planar substrates, where the entire NP solution breaks up into individual droplets to form ring patterns or islands upon drying[27]. Our observation showed that the one-dimensionality of NWs served as a guide in directing the uniform spatial arrangement of NP catalysts onto the NW surface, enabling easy and reproducible assembly of the CO_2 reduction photoelectrode with well-defined semiconductor-catalyst interface.

Scanning electron microscopy (SEM) images confirm the controllable uniform assembly of individual NPs with varying loading amounts (Figure 1c). The uniformity can be maintained even for very large surface coverage (Figure 1d). This is particularly important as it allows effective utilization of their nanoscale surface for catalysis. Scanning transmission electron microscopy (STEM) and elemental mapping (Figure 1e) further confirm the presence of uniformly distributed Au_3Cu NPs. In contrast, NP assembly on planar substrates with identical procedures typically resulted in the formation of islands where nanoparticles were aggregated (Extended Data Figure 3). Quantitative analysis of NPs on NW arrays reveals that the NP distribution along the NW showed a relatively higher coverage at the top (Extended Data Figure 4), which could be explained by the unidirectional drying process of the NP solution from the 3-dimensional NW geometry (Figure 1a and Extended Data Figure 5)[28,29]. Our hypothesis of particle

4

deposition with a receding meniscus suggests that the aspect ratio of the nanowires needs to be large enough to accommodate all the NPs in solution before the liquid front reaches the bottom part of the wires. With lower aspect ratio NWs, nearly half of the NPs settled to the base of the substrate (Extended Data Figure 6).

Light-driven CO_2 reduction on NP decorated planar and NW substrates was performed under 20 mW/cm^2 of 740 nm illumination to take into account CO_2 mass-transport limitations in CO_2-saturated 0.1 M $KHCO_3$ (Figure 2a)[30]. Under dark, both electrodes showed negligible current output. In contrast, greatly enhanced photocurrents were observed under illumination with both photoelectrodes exhibiting similar open-circuit voltage at around 0.25 V vs RHE, implying comparable photovoltage output. However, compared to the planar counterpart, NW substrate exhibited higher total current, which could be an indication of enhanced photoelectrochemical CO_2 reduction with lowered overpotentials (~130 mV difference at 1mA/cm^2 compared with the planar counterpart). NW substrates under chronoamperometry (Extended Data Figure 7) also showed enhanced steady-state photocurrents compared to the planar substrates.

As CO_2 reduction typically leads to various different products, the rate of individual product formation needs to be quantified to evaluate performance. Examination through gas chromatography and quantitative nuclear magnetic resonance spectroscopy on both types of photoelectrodes reveals CO as a major product. H_2 and a small amount of formate (Extended Data Figure 8) are detected as well. As shown in Figure 2a, NW photocathode exhibited faradaic efficiency (FE) of CO reaching close to 80% at only -0.20 V vs RHE (90 mV from the equilibrium potential for CO_2/CO), indicating 80% of the photogenerated charge extracted was used to selectively drive CO_2-

to-CO conversion at the catalyst end[14]. We also observed the FE reaching a peak and declining at moderate overpotentials, likely due to the mass transport limitations[30]. Partial current densities for CO (j_{CO}) were observed in the range from 2.2 to 3.8 mA/cm^2 for the NW photoelectrodes in between -0.20 V to -0.37 V vs RHE (Figure 2b). Compared to the planar counterpart showing j_{CO} from 0.6 to 1.8 mA/cm^2 within the same potential range, NW photoelectrodes exhibited performance with an average enhancement factor of 2.8. In other words, when evaluated in terms of additional bias (overpotential) needed to drive CO_2-to-CO conversion, NW photoelectrodes required less overpotentials (~120 mV lower) compared to the planar photoelectrodes. The NW geometry allows decreasing the photogenerated electron flux ($Flux_{e^-}$) over its large surface area (Figure 2c), alleviating the turnover requirement of the loaded catalyst and consequently reducing the necessary overpotential[31]. Compared to the planar substrate, NW array with high roughness factor in this work allows $Flux_{e^-}$ dilution by 14.25 times, when considering its entire surface area, as presented by the dotted lines in Figure 2c.

This is, however, the idealized case, to benefit the most from having a high surface area light-harvesting support when catalysts are spatially coupled, the interfaced catalysts have to be well-dispersed across the entire surface so that a large contact area is formed to distribute the electron flux, together with a large number of active sites exposed for catalytic turnover. Considering the real interfacial area determined by NP assembly on both photoelectrodes (with coverage values 7.30% and 24.9% on the NW and PL, respectively), it is also clear that NWs were favorable in this aspect by directing uniform assembly of nanoparticle catalysts from its one dimensionality, which resulted in a consistently reduced $Flux_{e^-}$ by a factor of 4 in comparison to that of the planar

substrates (solid lines in Figure 2c). In the case of maximal photogenerated electron extraction, the NP assembled NW photoelectrode exhibited reduced $Flux_{e^-}$ of 414 electrons/(nm^2·s) compared to that of the planar substrate with 1753 electrons/(nm^2·s). In addition, the effect of reduced overpotentials from electron flux dilution is further enhanced when the reaction under interest is sluggish with slow turnover and the relative increase in turnover is less per added overpotential. This is indeed the case for CO_2 reduction that requires greater amount of overpotential for turnover increase, especially in the operational current region (Extended Data Figure 9) for solar-to-fuel conversion to be practical. Therefore, NW photoelectrodes are clearly advantageous in reducing overpotential for CO_2 reduction compared to the well-known proton reduction, by allowing each catalyst to operate at a diluted electron flux. From the performance observed, we could see that the NW, as a light absorber, has allowed effective charge transport to the assembled NPs for CO_2 reduction without disturbing their inherent catalytic activity. More importantly, by utilizing the unique value of one-dimensionality present in the NW system that allowed uniform assembly, target products could be effectively synthesized with decrease of electrocatalytic losses in the form of kinetic overpotentials[32].

The integrated system was tested for an extended period of 18 hours (Figure 3a). As shown, with minimal change in current density, CO was maintained as a major product during continuous operation exhibiting long-term capability for photoelectrochemical CO_2 reduction[6–8]. Furthermore, we tried to see if a third component could be incorporated to enhance photoelectrochemical performance. Using the identical drop-casting approach, the addition of 1-butyl-3-methylimidazolium tetrafluoroborate

(BMIM-BF$_4$)[15] can further enhance the CO selectivity in the low overpotential region, with FE rising from 44.9% to 64.2% at -0.09 V vs RHE (Figure 3b). The adsorption of BMIM-BF$_4$ on NP catalyst surface allows lowering the energy barriers for CO$_2$ reduction by complexation with the CO$_2$ reduction intermediate, thereby leading to favorable charge transport toward CO$_2$ reduction rather than competing hydrogen evolution. This further illustrates how combining multiple components using the simple method described here could be effective for artificial photosynthesis.

Beyond the already proven benefits of Si NWs as an attractive material for photoelectrochemical applications[33,34], here, we have shown an additional advantage of the one-dimensional geometry allowing a simple and effective integration process for photoelectrochemical reduction of CO$_2$. The assembly process demonstrated here shows that Si NWs have the potential to perform as a general platform for interfacing a wide range of CO$_2$ reducing NP catalysts for light-driven applications. As part of the process in constructing a sophisticated system with optimized light harvesting and catalytic components, this approach will facilitate the advances of artificial photosynthesis combining synthetic nanoparticle catalysts.

Methods

Fabrication of the silicon nanowire array substrates. Wafer-scale silicon nanowire arrays were fabricated by deep reactive-ion etching (DRIE) method on photoresist-patterned single crystalline silicon wafers[10]. In a typical procedure, p-type boron-doped 6" Si wafer (<100> oriented, 1~5 Ohm·cm) was patterned with a dot array arranged on a square lattice with a 2 μm pitch using a standard photolithography stepper (GCA 8500). Then, this wafer underwent a low-frequency inductive-coupled plasma DRIE (STS Deep Silicon Etcher) process to produce nanowire arrays with uniform length ~22.5 μm and diameter ~850 nm. After removing the photoresist residue with O_2 plasma, ~100nm of dry thermal oxide shell was grown on the nanowires at 1050 ℃ for 100 min. 10:1 buffered hydrogen fluoride (BHF) was used to remove silicon oxide. Rinsed with H_2O (18.2 MOhm·cm resistivity) and acetone and dried under a stream of N_2 (g), the silicon nanowire arrays with diameter ~750 nm was obtained.

Fabrication of TiO_2-protected n^+p-Si PL and NW array substrates. To improve the photovoltage output[35], heavily arsenic-doped n^+ layer was formed on Si PL and NW substrate surface. A silicon handle wafer was first spin-coated with arsenic-containing spin-on dopant (SOD) (Filmtronics, Inc.) at 2200 rpm for 30 s and then baked at 150 ℃ on a hotplate for 30 min. Subsequently, Si PL and NW chips (both <100> oriented, boron-doped, 1~5 Ohm·cm) were placed upside down on the SOD-coated silicon handle wafer and subjected to rapid thermal annealing (RTA) at 900 ℃ for 3 min in N_2 atmosphere. These chips were taken out carefully from RTA chamber after cooling down under a N_2 ambient and soaked into 10:1 BHF for ~30 s to remove the thin oxide formed during n^+ doping process. After that, these chips were rinsed with H_2O (18.2 MOhm·cm resistivity) and acetone and dried under N_2 (g) stream. Finally, these n^+p-Si PL and NW chips were immediately transferred into an ALD (atomic layer deposition, Picosun ALD system) chamber. Thin TiO_2 layer (10 nm) was uniformly coated onto the surface to protect substrates from corrosion in the following photoelectrochemical measurement.

Synthesis and characterization of Au_3Cu NP. Au_3Cu NPs were synthesized via the co-reduction of both metal precursors. First, 20ml of 1-octadecene was heated to 130°C under nitrogen atmosphere. After cooling back to room temperature, 2mmol of oleic acid, 2mmol of oleylamine, 0.6mmol of gold acetate, 0.2mmol of copper acetate and 4mmol of 1,2-hexadecanediol were added. Under the inert atmosphere, the mixture was heated to 200°C and kept at that temperature for 2 h while stirring. Afterwards, it was further heated to 280°C for 1 h. Then, the reaction was stopped by cooling it down to room temperature. Ethanol was added to the mixture to precipitate the synthesized nanoparticles and was washed once more with hexane and ethanol by centrifugation. NPs

were characterized by XRD (Bruker D8), TEM (Hitachi H-7650), UV-Vis spectroscopy (Vernier) and ICP-AES (PerkinElmer Optima 7000 DV).

Assembly of Au₃Cu NPs on Si PL and NW substrates. 90 μL of Au₃Cu NP solution was added to 210 μL hexane and sonicated for 15 s. Then, different amounts of the solution (18 μL is denoted as x1 loading with NP loading mass of 4 μg. x2 to x10 represents proportionally increased loading amounts.) were drop-casted on 0.8 cm * 0.8 cm TiO$_2$-protected n$^+$p-Si PL and NW array square pieces and dried spontaneously. Surfactant residues were removed by soaking square pieces into pure acetic acid for 90 s, followed by immersing into N, N-Dimethylmethanamide (DMF) for 1 min and subsequently into ethanol for 15 s. Finally, all Si PL and NW array square pieces with Au₃Cu NP loading were dried under N$_2$ stream. x2 loading was used to demonstrate photoelectrochemical reduction of CO$_2$.

NP coverage on NW substrates was analyzed by counting the number of particles and measuring the size of each particle in a given area using particle analysis of imageJ. Multiple measurements were performed at different regions across the substrate and NWs were sectioned into eight segments along the wire axis to perform quantitative analysis along the entire length.

Au₃Cu-n$^+$p-Si NW photoelectrode with ionic liquid (IL) addition. Photoelectrodes with ionic liquid (1-Butyl-3-methylimidazolium tetrafluoroborate (BMIM-BF$_4$)) added were prepared by following a similar way as preparing Au₃Cu-n$^+$p-Si NW array substrates. 0.1 μL BMIM-BF$_4$ was mixed with 8 mL hexanes and 10 μL of the mixture was drop-casted onto Au₃Cu-n$^+$p-Si NW array substrates after made.

Electrode fabrication. Photoelectrodes were fabricated on both Au₃Cu NP assembled n$^+$p-Si PL and NW array substrates. Ohmic contact was made by rubbing Ga-In eutectic on the back side of the square pieces. Electrical connections were made by fixing these square pieces on Ti foil with conductive silver paint and carbon tape. Finally, nail polish was used to seal the square pieces and define the active area of the photoelectrode.

Photoelectrochemical (PEC) measurements. All PEC measurements were carried out in our customized PEC setup. Two compartments of the cell are separated by an anion exchange membrane (Selemion AMV). A Pt wire was used as a counter electrode and Ag/AgCl (in 1 M KCl) as a reference electrode. Au₃Cu-n$^+$p-Si PL and NW electrodes were transferred inside the cell to test CO$_2$ reduction performance. 0.1 M KHCO$_3$ electrolyte solution was pre-electrolyzed for >16 h. Electrolyte (27.5 mL in the working compartment with gas headspace ~5 mL) was added into the cell, which was saturated with CO$_2$ (Praxair, 5.0 Ultra high purity) for 20 min at a flow rate of 30 mL min^{-1} under

stirring. All the electrolysis was conducted under the illumination (LED light source with intensity 20 mW cm^{-2}, wavelength λ = 740 nm, calibrated with a standard Si photodiode) at room temperature and 1 atm CO_2 with electrolyte pH at 6.8. Each measurement was conducted multiple times to check the consistency of our experiments. Electrochemical data presented in this work are the average values out of these multiple measurements and error bars are one times the standard deviation.

During chronoamperometry, effluent gas from the cell went through the sampling loop of a gas chromatograph (SRI) to analyze the concentration of gas products. The gas chromatograph was equipped with a molecular sieve 13X and hayesep D column with Ar (Praxair, 5.0 Ultra high purity) flowing as a carrier gas. The separated gas products were analyzed by a thermal conductivity detector (for H_2) and a flame ionization detector (for CO). Quantification of the products was performed with the conversion factor derived from the standard calibration gases. To avoid any issues related to gas product detection, such as large fluctuations in the total amount being observed at each measurement point and detection efficiency varying with the total amount of current being generated, faradaic efficiencies of the products were normalized with the sum being unity.

Liquid products were analyzed afterwards by qNMR (Bruker AV-500) using dimethyl sulfoxide as an internal standard. Solvent presaturation technique was implemented to suppress the water peak. Faradaic efficiencies were calculated from the amount of charge passed to produce each product divided by the total charge passed at a specific time or during the overall run.

Author contributions

References

1. White, J. L. *et al.* Light-Driven Heterogeneous Reduction of Carbon Dioxide: Photocatalysts and Photoelectrodes. *Chem. Rev.* **115,** 12888-12935 (2015).

2. Kim, D., Sakimoto, K. K., Hong, D. & Yang, P. Artificial Photosynthesis for Sustainable Fuel and Chemical Production. *Angew. Chemie Int. Ed.* **54,** 3259–3266 (2015).

3. Schreier, M. *et al.* Coordinative immobilization of a molecular catalyst on Cu_2O photocathodes for CO_2 reduction. *J. Am. Chem. Soc.* **138,** 1938-1946 (2016).

4. Liu, C. *et al.* Nanowire–bacteria hybrids for unassisted solar carbon dioxide fixation to value-added chemicals. *Nano Lett.* **15,** 3634-3639 (2015)

5. Woolerton, T. W. *et al.* Efficient and clean photoreduction of CO_2 to CO by enzyme-modified TiO_2 nanoparticles using visible light. *J. Am. Chem. Soc.* **132,** 2132–2133 (2010).

6. Barton, E. E., Rampulla, D. M. & Bocarsly, A. B. Selective solar-driven reduction of CO2 to methanol using a catalyzed p-GaP based photoelectrochemical cell. *J.*

Am. Chem. Soc. **130,** 6342–6344 (2008).

7.   Qiu, J. *et al.* Artificial photosynthesis on TiO_2- passivated InP nanopillars. *Nano Lett.* **15,** 6177-6181 (2015).

8.   Choi, S. K. *et al.* Sn-coupled p-Si nanowire arrays for solar formate production from CO_2. *Adv. Energy Mater.* **4,** 1301614 (2014).

9.   Liu, C., Dasgupta, N. P. & Yang, P. Semiconductor nanowires for artificial photosynthesis. *Chem. Mater.* **26,** 415–422 (2014).

10.   Liu, C., Tang, J., Chen, H. M., Liu, B. & Yang, P. A fully integrated nanosystem of semiconductor nanowires for direct solar water splitting. *Nano Lett.* **13,** 2989–2992 (2013).

11.   Mayer, M. T., Du, C. & Wang, D. Hematite/Si nanowire dual-absorber system for photoelectrochemical water splitting at low applied potentials. *J. Am. Chem. Soc.* **134,** 12406–12409 (2012).

12.   Boettcher, S. W. *et al.* Photoelectrochemical hydrogen evolution using Si microwire arrays. *J. Am. Chem. Soc.* **133,** 1216–1219 (2011).

13.   Gao, D. *et al.* Size-dependent electrocatalytic reduction of CO_2 over Pd nanoparticles. *J. Am. Chem. Soc.* **137,** 4288-4291 (2015).

14.   Kim, D., Resasco, J., Yu, Y., Asiri, A. M. & Yang, P. Synergistic geometric and electronic effects for electrochemical reduction of carbon dioxide using gold-copper bimetallic nanoparticles. *Nat. Commun.* **5,** 4948 (2014).

15.   Zhu, W. *et al.* Monodisperse Au nanoparticles for selective electrocatalytic reduction of CO_2 to CO. *J. Am. Chem. Soc.* **135,** 16833–16836 (2013).

16.   Dai, P. *et al.* Solar hydrogen generation by silicon nanowires modified with

platinum nanoparticle catalysts by atomic layer deposition. *Angew. Chem. Int. Ed.* **52,** 11119–11123 (2013).

17. Paracchino, A., Laporte, V., Sivula, K., Grätzel, M. & Thimsen, E. Highly active oxide photocathode for photoelectrochemical water reduction. *Nat. Mater.* **10,** 456–461 (2011).

18. Tilley, S. & Schreier, M. Ruthenium oxide hydrogen evolution catalysis on composite cuprous oxide water splitting photocathodes. *Adv. Funct. Mater.* **24,** 303-311 (2014).

19. Reece, S. Y. *et al.* Wireless solar water splitting using silicon-based semiconductors and earth-abundant catalysts. *Science* **334,** 645–648 (2011).

20. Hou, Y. *et al.* Bioinspired molecular co-catalysts bonded to a silicon photocathode for solar hydrogen evolution. *Nat. Mater.* **10,** 434–438 (2011).

21. AlOtaibi, B., Fan, S., Wang, D., Ye, J., & Mi, Z. Wafer-level artificial photosynthesis for CO_2 reduction into CH_4 and CO using GaN nanowires. *ACS Catal.* **5,** 5342-5348 (2015).

22. Torralba-Peñalver, E., Luo, Y., Compain, J.-D., Chardon-Noblat, S. & Fabre, B. Selective catalytic electroreduction of CO_2 at silicon nanowires (SiNWs) photocathodes using non-noble metal-based manganese carbonyl bipyridyl molecular catalysts in solution and grafted onto SiNWs. *ACS Catal.* **5,** 6138–6147 (2015).

23. Schreier, M. *et al.* Efficient photosynthesis of carbon monoxide from CO_2 using perovskite photovoltaics. *Nat. Commun.* **6,** 7326 (2015).

24. Delacourt, C., Ridgway, P. L., Kerr, J. B. & Newman, J. Design of an

electrochemical cell making syngas (CO + H$_2$) from CO$_2$ and H$_2$O reduction at room temperature. *J. Electrochem. Soc.* **155,** B42-B49 (2008).

25.	Zhan, Z. et al. Syngas production by coelectrolysis of CO$_2$/H$_2$O: the basis for a renewable energy cycle. *Energy & Fuels* **23,** 3089-3096 (2009).

26.	Jiao, F. et al. Selective conversion of syngas to light olefins. *Science* **351,** 1065-1068 (2016).

27.	Yunker, P. J., Still, T., Lohr, M. A. & Yodh, A. G. Suppression of the coffee-ring effect by shape-dependent capillary interactions. *Nature* **476,** 308–311 (2011).

28.	Chi, L. F., Gleiche, M. & Fuchs, H. Nanoscopic channel lattices with controlled anisotropic wetting. *Nature* **403,** 173–175 (2000).

29.	Huang, J., Kim, F., Tao, A. R., Connor, S. & Yang, P. Spontaneous formation of nanoparticle stripe patterns through dewetting. *Nat. Mater.* **4,** 896–900 (2005).

30.	Kuhl, K. P. *et al.* Electrocatalytic Conversion of carbon dioxide to methane and methanol on transition metal surfaces. *J. Am. Chem. Soc.* **136,** 14107–14113 (2014).

31.	Su, Y. *et al.* Single nanowire photoelectrochemistry. *Nat. Nanotech.* in press (2016).

32.	Walter, M. G. *et al.* Solar water splitting cells. *Chem. Rev.* **110,** 6446–73 (2010).

33.	Boettcher, S. W. *et al.* Energy-conversion properties of vapor-liquid-solid-grown silicon wire-array photocathodes. *Science* **327,** 185–187 (2010).

34.	Kelzenberg, M. D. *et al.* Enhanced absorption and carrier collection in Si wire arrays for photovoltaic applications. *Nat. Mater.* **9,** 239–244 (2010).

15

Reference in Methods and Extended data figures:

35. Warren, E. L., Boettcher, S. W., Walter, M. G., Atwater, H. A. & Lewis, N. S. Through use of radial n⁺p-Si junction microwire array photoelectrodes. *J. Phys. Chem. C* **115,** 594–598 (2011).

36. Murakami, D., Jinnai, H. & Takahara, A. Wetting transition from the cassie-baxter state to the wenzel state on textured polymer surfaces. *Langmuir* **30,** 2061–2067 (2014).

Figure Caption

Figure 1 | Au₃Cu NP assembly on Si NW arrays. (**a**) Schematic of the nanoparticle assembly process and the use of the integrated system for light-driven CO_2 reduction. (**b**) SEM image (scale bar 2 μm) of Au₃Cu NP assembled Si NW arrays. (**c**) SEM images (scale bar 200 nm) demonstrating uniform and tunable NP assembly on Si NW arrays. Numbers indicate loading amounts that have been proportionally varied. (**d**) Zoom-in image (scale bar 200 nm) of a Si NW with x10 loading of Au₃Cu NPs uniformly assembled. (**e**) STEM image and elemental mapping of Au (green), Cu (red) and Si (blue). Though the thick diameter of the Si NW suppresses the contrast of Au and Cu signals to background, we can clearly see the signals originating from the NPs at the edge of the NW. Scale bars are 200 nm.

Figure 2 | Photoelectrochemical reduction of CO_2 using integrated photoelectrodes. (**a**) Comparison between Au₃Cu NP assembled Si PL and NW photoelectrodes in catalytic activity and FE for CO_2 conversion to CO. Solid lines present linear sweep

voltammetry (10 mV s^{-1}) of both substrates under dark and under illumination. Each point represents total current density from the geometric area of the photoelectrodes during chronoamperometry and the numbers indicate faradaic efficiency towards CO. (**b**) Partial current density for CO generation of Au$_3$Cu NP assembled substrates and enhancement of NW over PL for comparison. All the measurements were under 20 mW/cm^2 of 740 nm illumination (calibrated with standard Si photodiode) with photon flux above silicon band gap comparable to one third of that obtained from 100 mW/cm^2, air mass 1.5 solar illumination to take into account CO_2 mass-transport limitations in 0.1 M KHCO$_3$ (pH = 6.8) at 1atm CO_2 and room temperature. Error bars at each potential are based on multiple measurements. (**c**) Estimation of photogenerated electron fluxes (Flux$_{e^-}$) over the output current range on both substrates. Flux$_{e^-}$ considering substrate total surface area (dashed line) and substrate/catalyst interfacial area (solid line) are both calculated. The flux$_{e^-}$ considering PL total surface area around the saturated photocurrent (~ 430 electrons/(nm^2·s)) matches well with the typical value of planar n$^+$p-Si (~ 1200 electrons/(nm^2·s) under one-sun illumination[31], and corrected by photon flux used in this work.). When considering the real interfacial area determined by NP assembly on both substrates, quantitative analysis of NP coverage (7.30% and 24.9% on NW and PL, respectively) is used. The inset shows NW substrate dimensions used for calculation.

Figure 3 | Photoelectrochemical performance in the long term and incorporating ionic liquid as a third component (**a**) CO_2 reduction activity of Au$_3$Cu NP/Si NW photoelectrode for 18 hours. Total current density and FE for CO at -0.26 V vs RHE. (**b**)

Potential-dependent CO FEs of Au$_3$Cu NP/Si NW photoelectrode incorporating ionic liquid BMIM-BF$_4$. All the data were obtained in CO$_2$-saturated 0.1 M KHCO$_3$ (pH = 6.8).
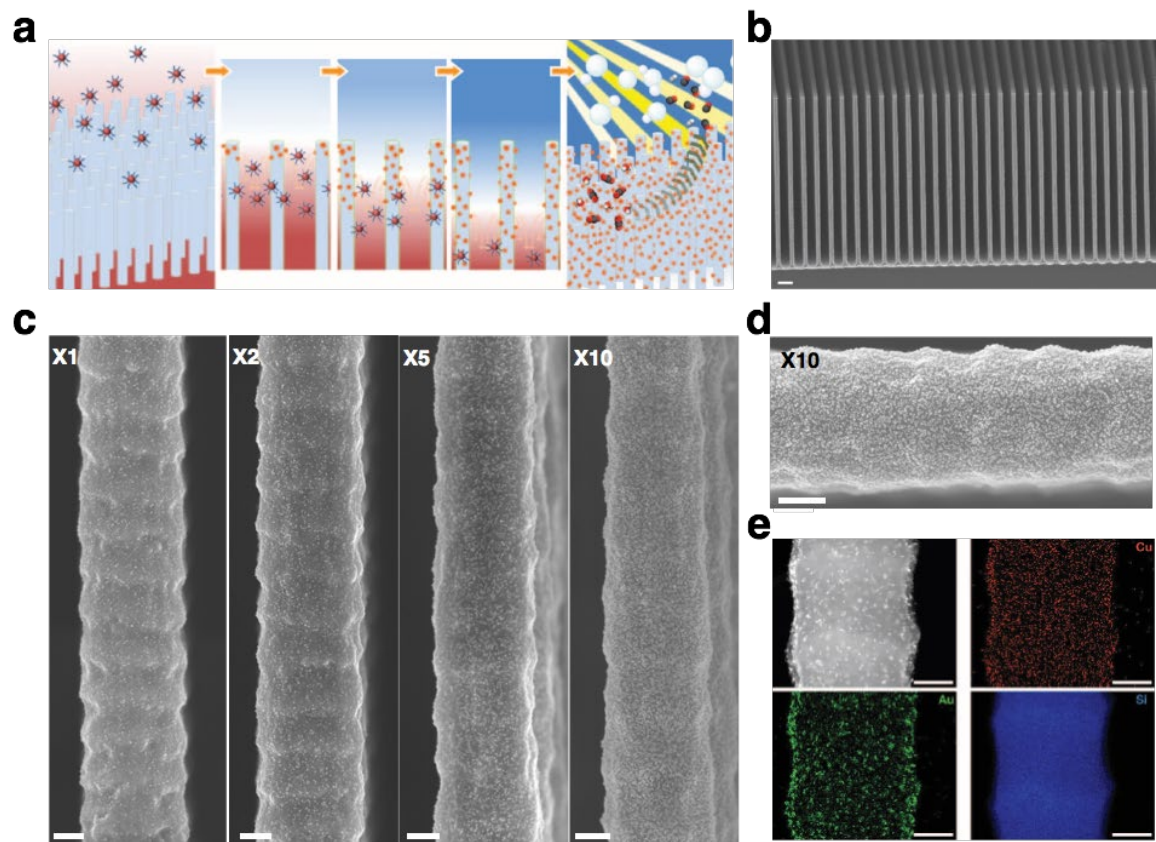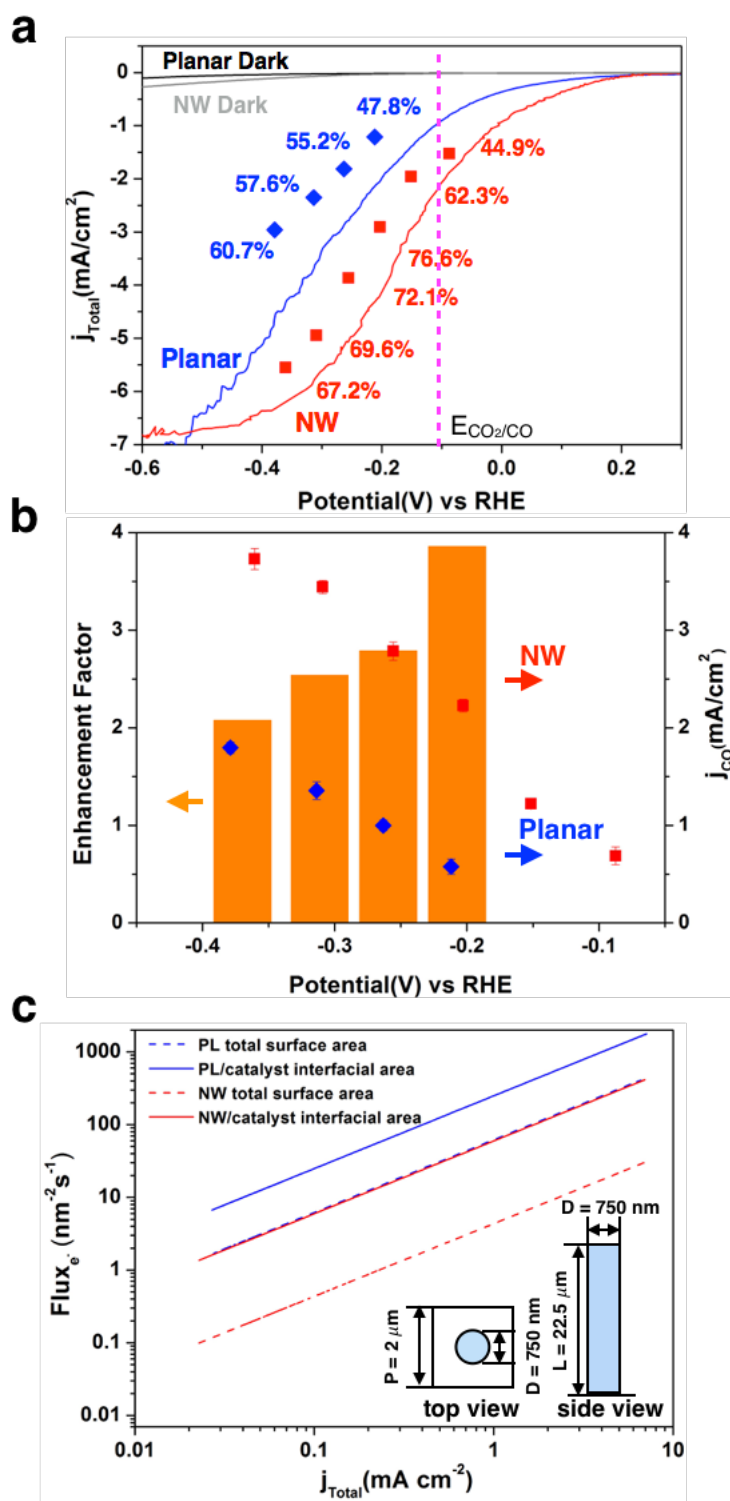
Figure 1.

Figure 2.

Figure 3.